

Inverse Design of Metal Nanoparticles' Morphology

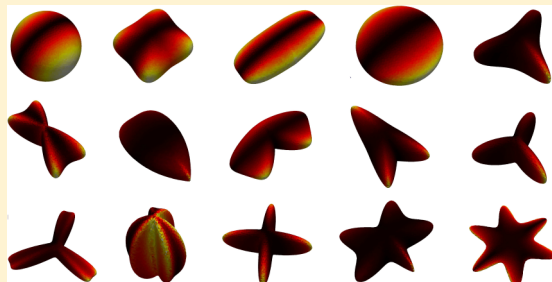
Carlo Forestiere,^{*,†} Yanyan He,[‡] Ren Wang,[§] Robert M. Kirby,^{*,||} and Luca Dal Negro^{*,§}

[†]Department of Electrical Engineering and Information Technology, Università degli Studi di Napoli Federico II, via Claudio 21, Napoli, 80125, Italy

[‡]Scientific Computing and Imaging Institute and ^{||}School of Computing, University of Utah, Salt Lake City, Utah 84112, United States

[§]Department of Electrical and Computer Engineering and Photonics Center, Boston University, 8 Saint Mary's Street, Boston, Massachusetts 02215, United States

ABSTRACT: The current praxis of designing plasmonic devices by hand, mainly guided by qualitative arguments, often derived from simplified semianalytical theories, significantly limits the accessible design space and, consequently, the achievable performances. In the present work, we propose a rigorous inverse design method to engineer three-dimensional metal nanoparticles according to a preassigned objective function, coupling an efficient global optimization algorithm to a full-retarded, electromagnetic solver based on the surface integral equation method. Thus, we use the proposed strategy to design the morphology of metal nanoparticles, maximizing the electric field average on their surface. We performed the optimization by varying the exciting wavelength in the ultraviolet and visible spectral ranges and the particle's material among the most used plasmonic materials, namely, gold, silver, and aluminum, obtaining different corresponding optimal shapes. General design criteria of nanoparticle's shape and size for best enhancement of electric fields are obtained. The automation of nanoparticles design enables the engineering of numerous nanoscale optical devices such as plasmon-enhanced Raman sensors, photodetectors, light sources, and more efficient nonlinear optical elements for on chip integration.



KEYWORDS: *localized surface plasmons, optimization, field enhancement, metal nanoparticles, nanoantennas, surface-enhanced Raman scattering (SERS)*

The recent numerous discoveries in plasmonics, driven by the advancements in nanofabrication and characterization techniques, require to renovate the traditional electromagnetic design paradigm, often dominated by antennas and waveguides principles. Specific and rigorous strategies for the design of metal nanostructures are not yet fully established. The few design methods that have stood out so far include, for instance, the plasmon hybridization¹ which is rooted in the electro quasi-static approximation (EQS) of the Maxwell's equations, and the adiabatic nanofocusing based on the eikonal (WKB) approximation.² Nevertheless, the geometries suggested by these approaches require additional refinements by a full-wave electromagnetic solver, carried out by sweeping the relevant geometrical parameters through a given range. This time-consuming design process exacerbates the delay between proof of concept plasmonic devices and marketable technology, which has become apparent in the past few years. On the other hand, the automation of the plasmonic design by rigorous *inverse-design* strategies could make very large search spaces easily accessible, where the user could look for a specific nanostructure meeting specific needs with unparalleled accuracy. Contrary to the solution of a *direct problem*, which simply aims at determining the electromagnetic field scattered by a given particle of prescribed shape, size, and composition under assigned excitation conditions, the *inverse-design* problem

consists of determining the characteristics of the scattering object, based on the desired properties of the scattered electromagnetic field.

Currently, the inverse design of nanoplasmonic structures is still in its embryonic stages, mainly due to the difficulties in solving inverse electromagnetic problems with a large number of degrees of freedom, which requires the coupling of efficient optimization codes with full-wave electromagnetic solvers of high numerical accuracy, especially in the near field region. For these reasons, several research groups have so far sidestepped the full inverse problem, either by resorting to approximated electromagnetic solvers or by drastically limiting the search space. For instance, in ref 3, the authors coupled a particle-swarm optimization to an electromagnetic solver based on the single-dipole-approximation to design metal nanoparticle arrays with broadband field enhancement. This work treats very large arrays of interacting particles, each of them is modeled by a sphere much smaller than the incident wavelength. In ref 4, a two-dimensional electroquasistatic (EQS) numerical code, that completely neglects retardation effects, was coupled to an optimization algorithm in order to design the spectral

Received: August 19, 2015

Published: December 8, 2015

resonance position of a deep-subwavelength plasmonic cylinder of arbitrary cross section. In ref 5, the authors coupled a genetic algorithm with a full-retarded solver based on the multiparticles Mie theory to maximize the field enhancement exhibited by an array of 3D plasmonic spheres. In refs 6 and 7, the authors coupled an optimization algorithm to a full-retarded 2D boundary-element method solver to optimize an infinite plasmonic cylinder whose cross section is described by the Gielis' superformula. However, the optimization of a translational invariant plasmonic structure, although interesting in principle, has a very limited applicability. The only plasmonic scatterer that can be successfully modeled in two dimension is a metal nanowire. On the contrary, the scattering from a plasmonic nanoparticle is inherently three-dimensional since the three geometrical dimensions of a typical metal nanoparticle are comparable and the use of 3D numerical methods is therefore mandatory. An advance toward the realization of a fully automatic plasmonic design is represented by the work of Feichtner et al.⁸ They coupled an evolutionary optimization with a 3D finite-difference-time-domain (FDTD) to tile a checkerboard of 20×20 discrete gold cubes with 10 nm edge to form a 3D plasmonic nanoantenna with maximum field enhancement. Unfortunately, a checkerboard of cubes with 10 nm edge poorly approximates arbitrary 3D shapes. Moreover, the FDTD method is not fully reliable to accurately compute local electromagnetic fields in plasmonic nanostructures.^{9,10} In fact, FDTD suffers from numerical dispersion¹¹ and, when strong field localization is present, it displays a very poor converge in comparison to other methods.¹⁰ This fact may lead to spurious solutions of the inverse scattering problem.

In the present work, we propose the rigorous inverse design of the shape of three-dimensional (3D) metal nanoparticles, aiming at the maximization of an assigned objective function in a *continuous* parameter space. We tackle the inverse problem by coupling an efficient global optimization algorithm (EGO)^{12,13} with a fully retarded, electromagnetic solver based on a surface integral formulation of Maxwell's equations^{14,15} that, unlike FDTD, guarantees high accuracy in the near field region,¹⁶ allowing the reliable optimization of near-field quantities. Differently from ref 8, not only did we exploit a more accurate electromagnetic solver, but also implemented the optimization on a much larger set of 3D shapes generated using Gielis' superformula¹⁷ with a *continuous* parameter space, where the values of the shape parameters belong to a hypercube rather than to a discrete set.

Depending on the application, different objective functions could be chosen. In particular, the optimization of *far-field* synthetic parameters such as the scattering, absorption, or extinction efficiencies, may help scientist and engineers conceive novel plasmonic nanosensors with enhanced sensitivity and minimum losses. Likewise, the reverse engineering of *near-field* quantities may also boost the performance of many plasmonic devices. For instance the maximization of the local electric field is critical for the improvement of subwavelength light concentrators and Surface Enhanced Raman Scattering (SERS) substrates,¹⁸ whereas the reverse engineering of the local density of states (LDOS) or the Purcell factor could suggest unanticipated strategies for accelerating spontaneous decay rates at optical frequencies and for tailoring light-matter interactions.¹⁹ Due to its chief importance in Plasmonics, we chose to optimize the near field enhancement averaged over the particle surface. Implementing the notation used by Moskovits in ref 18, we call this quantity g . The

quantity g plays a chief role in the electromagnetic theory^{20–22} of SERS, being the intensity of the SERS-scattered field given by

$$I_{\text{SERS}} = |\alpha_S|^2 |g(\lambda_0)g(\lambda_R)|^2 I_0 \quad (1)$$

where α_S is a combination of components of the Raman tensor, I_0 is the intensity of the incident field, $g(\lambda_0)$ and $g(\lambda_R)$ represent the value of g at the pump wavelength λ_0 and at the Raman-shifted wavelength λ_R . In particular, for low-frequency bands, since $g(\lambda_0) \approx g(\lambda_S)$ we have with a good approximation:

$$I_{\text{SERS}} \approx |\alpha_S|^2 |g(\lambda_0)|^4 I_0 \quad (2)$$

It is apparent that the maximization of I_{SERS} is mathematically equivalent to the maximization of the average local near field at the particle surface, namely, $g(\lambda)$. Besides SERS, strongly enhanced local field values are required in almost all practical applications of plasmonics, including nonlinear plasmonics,²³ plasmon-enhanced photodetectors²⁴ and solar cells,²⁵ optical manipulators,²⁶ modulators,²⁷ thermal emitters,²⁸ aperture-less near-field scanning optical microscopy,²⁹ and heat-assisted magnetic recording.³⁰

■ FORMULATION OF THE PROBLEM

Let us now formulate the inverse design problem for the monochromatic linear electromagnetic scattering by a single homogeneous and isotropic nanoparticle. The domain of the electromagnetic field is the entire space \mathbb{R}^3 , which is divided by the smooth surface Σ , representing the particle's boundary, into the interior of the dielectric domain $\Omega^{(i)}$, that is the particle volume, and the external medium $\Omega^{(e)}$. The quantities ϵ_i and ϵ_e denote the linear permittivity of the particle and of the embedding medium, respectively. It is apparent that a homogeneous and isotropic nanoparticle is completely specified by Σ and ϵ_i . They are, in principle, the unknowns of the inverse scattering problem. Furthermore, we denote with $(\mathbf{E}_0, \mathbf{H}_0)$ the external field at wavelength λ , and with $(\mathbf{E}^{(i)}, \mathbf{H}^{(i)})$ and $(\mathbf{E}^{(e)}, \mathbf{H}^{(e)})$ the total fields in $\Omega^{(i)}$ and $\Omega^{(e)}$, respectively. We can define the scattered fields $(\mathbf{E}_S^{(i)}, \mathbf{H}_S^{(i)})$ and $(\mathbf{E}_S^{(e)}, \mathbf{H}_S^{(e)})$ as

$$\begin{aligned} \mathbf{E}_S^{(i)} &= \mathbf{E}^{(i)} & \mathbf{E}_S^{(e)} &= \mathbf{E}^{(e)} - \mathbf{E}_0 & \text{in } \Omega^{(i)}, \quad \text{in } \Omega^{(e)} \\ \mathbf{H}_S^{(i)} &= \mathbf{H}^{(i)} & \mathbf{H}_S^{(e)} &= \mathbf{H}^{(e)} - \mathbf{H}_0 \end{aligned} \quad (3)$$

The scattered fields have to satisfy the following equations (a time-harmonic dependence $e^{j\omega t}$ has been assumed, where j is the imaginary unit):

$$\begin{aligned} \nabla \times \mathbf{E}_S^{(t)} &= -j\omega\mu_0\mathbf{H}_S^{(t)} & \text{in } \Omega^{(t)}, \quad \text{with } t = i, e \\ \nabla \times \mathbf{H}_S^{(t)} &= j\omega\epsilon_t\mathbf{E}_S^{(t)} \end{aligned} \quad (4)$$

$$\begin{aligned} \mathbf{n} \times (\mathbf{H}_S^{(e)} - \mathbf{H}_S^{(i)}) &= -\mathbf{n} \times \mathbf{H}_0 & \text{on } \Sigma \\ \mathbf{n} \times (\mathbf{E}_S^{(e)} - \mathbf{E}_S^{(i)}) &= -\mathbf{n} \times \mathbf{E}_0 \end{aligned} \quad (5)$$

which have to be solved with the radiation condition at infinity.

In this work, we measure the performance of a metal nanoparticle in terms of the averaged electric-field enhancement on the surface Σ , namely:

$$g(\lambda) = \frac{1}{|\Sigma|} \iint_{\Sigma} \left\| \frac{\mathbf{E}^{(e)}}{\mathbf{E}_0} \right\| dS \quad (6)$$

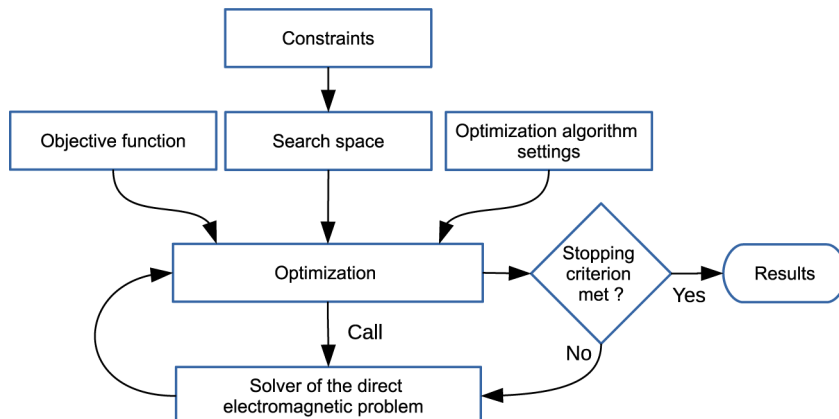


Figure 1. Flowchart of a general optimization scheme for the solution of inverse design problems.

Moreover, we restrict our inverse design only to the particle's shape and size, setting the permittivity ϵ_i equal to that of real world metals, that is, gold, silver, or aluminum. This is because, although at microwaves or at the far-infrared particles exhibiting a prescribed macroscopic value of permittivity can be fabricated using metamaterials (e.g., ref 31), at optical frequencies this is extremely challenging due to the difficulties in assembling strongly subwavelength meta-elements. We also assume the external medium to have the permittivity of air, that is, $\epsilon_e = \epsilon_0$.

In conclusion, our goal is to find the optimal surface morphology Σ of a homogeneous and isotropic particle of assigned permittivity ϵ_i that, excited by the external field ($\mathbf{E}_0, \mathbf{H}_0$) at wavelength λ , determines in the space an electromagnetic field that solves the problem of [eqs 4](#) and [5](#) and simultaneously maximizes the quantity g .

The typical scheme to tackle this problem follows the workflow shown in [Figure 1](#). First, we have to choose the objective function and specify the search space where we look for the best solution. The search space may be limited by suitable constraints depending, for instance, on the physical realizability of the scatterer with the available fabrication tools. Then, we seek out the solution of the inverse problem by iteratively coupling an optimization algorithm with an electromagnetic solver. Eventually, the optimization loop is terminated once a convenient stopping criterion has been met.

Therefore, three main issues have to be addressed: (i) how to describe the nanoparticle's surface Σ in terms of several parameters that define the search space; (ii) how to accurately and efficiently solve the direct electromagnetic problem; (iii) how to solve the inverse problem. The methods by which we deal with these challenges will be presented in the following paragraphs. It is also worth noting that the present formulation can be easily extended to design the geometry of an array of several interacting particles maximizing multiple objective functions.

MORPHOLOGICAL DESCRIPTION

We parametrically describe the closed boundary Σ of the metal nanoparticle by using a simple, unifying equation, the superformula. J. Gielis introduced its mathematical expression about a decade ago¹⁷ and proved it to be extremely effective to describe a variety of forms and patterns occurring in nature, including cells, tissues, stems, flowers, shells, starfish, galaxies, and DNA molecules.³² The importance of the superformula in inverse engineering was envisioned by Gielis himself,³³ and it was already used for the synthesis of RF-antennas.³⁴ It was first

introduced in Plasmonics by Rodríguez-Oliveros and Sánchez-Gil to describe the shape of 3D plasmonic nanoparticles³⁵ and, in its 2D form, was also used for the inverse design of translational-invariant plasmonic cylinders.^{6,7} The Gielis' superformula in three dimensions has the mathematical expression:

$$\begin{aligned} x &= \eta r_1(\phi) \cos(\phi) r_2(\theta) \cos(\theta) \\ y &= \eta r_1(\phi) \sin(\phi) r_2(\theta) \cos(\theta) \\ z &= \eta r_2(\theta) \sin(\theta) \end{aligned} \quad (7)$$

where

$$\begin{aligned} r_1(\phi) &= \left[\left| \frac{\cos\left(\frac{m(\phi)}{4}\phi\right)}{a^{(\phi)}} \right|^{n_1^{(\phi)}} + \left| \frac{\sin\left(\frac{m(\phi)}{4}\phi\right)}{b^{(\phi)}} \right|^{n_3^{(\phi)}} \right]^{-1/n_1^{(\phi)}} \\ r_2(\theta) &= \left[\left| \frac{\cos\left(\frac{m(\theta)}{4}\theta\right)}{a^{(\theta)}} \right|^{n_1^{(\theta)}} + \left| \frac{\sin\left(\frac{m(\theta)}{4}\theta\right)}{b^{(\theta)}} \right|^{n_3^{(\theta)}} \right]^{-1/n_1^{(\theta)}} \end{aligned} \quad (8)$$

and $\theta \in [-\pi/2, \pi/2]$, $\phi \in [-\pi, \pi]$. From [eqs 7](#) and [8](#) it is apparent that the superformula can be completely described by 13 parameters, six of them, that is, $m^{(\phi)}, n_1^{(\phi)}, n_2^{(\phi)}, n_3^{(\phi)}, a^{(\phi)}$, and $b^{(\phi)}$ modulate the shape along the azimuthal angle ϕ , while the parameters $m^{(\theta)}, n_1^{(\theta)}, n_2^{(\theta)}, n_3^{(\theta)}, a^{(\theta)}$, and $b^{(\theta)}$ control the variation of the shape along the altitude angle θ (zenith). The remaining parameter η controls the scaling of the resulting shape. However, being interested in shapes compatible with *planar* nanofabrication technology we keep fixed the altitude parameters:

$$\begin{aligned} m^{(\theta)} &= 2; \\ n_i^{(\theta)} &= 2 \quad \forall i = 1, 2, 3; \\ a^{(\theta)} &= b^{(\theta)} = 1 \end{aligned} \quad (9)$$

Moreover, in order to exclude from the optimization space shapes with extremely sharp edges we impose the following constraints on the azimuthal parameters:

$$\begin{aligned}
 1 &\leq m^{(\phi)} \leq 8; \\
 0.75 &\leq n_i^{(\phi)} \leq 6 \quad \forall i = 1, 2, 3; \\
 0.25 &\leq a^{(\phi)} \leq 2; \\
 0.25 &\leq b^{(\phi)} \leq 2
 \end{aligned} \tag{10}$$

Finally, in order to avoid excessively small or large particles we also set constraints on the scaling factor η :

$$25 \times 10^{-9} \leq \mu \leq 75 \times 10^{-9} \tag{11}$$

In conclusion, we have reduced the inverse problem of designing the nanoparticle shape to a constrained optimization with respect to only seven parameters. Figure 2 illustrates

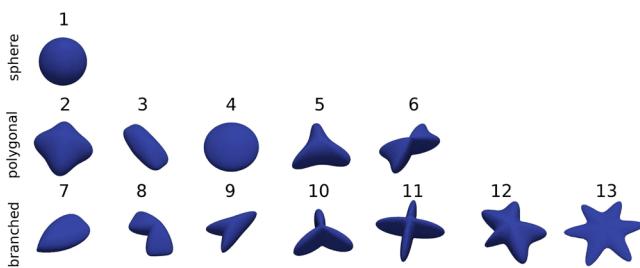


Figure 2. Exemplificative shapes generated by the 3D Gielis superformula, namely, (1) nanosphere, (2) nanosquare, (3) nanorod, (4) nanodisk, (5) nanotriangle, (6) bow-tie, (7) monopod, (8) bipod, (9) nanoarrow, (10) tripod, (11) tetrapod, (12) pentapod, and (13) hexapod.

several exemplificative shapes that can be generated using the 3D superformula, with the constraints specified by eqs 9 and 10; their parameters are listed in Table 1. We conveniently

Table 1. Superformula Parameters Describing the Exemplificative Shapes Shown in Figure 2

	$m^{(\phi)}$	$n_1^{(\phi)}$	$n_2^{(\phi)}$	$n_3^{(\phi)}$	$a^{(\phi)}$	$b^{(\phi)}$
nanosphere	2.00	2.00	2.00	2.00	1.00	1.00
nanosquare	3.96	2.64	3.68	4.65	1.14	1.14
nanorod	4.08	3.52	3.15	5.35	1.28	1.91
nanodisk	2.00	2.00	2.00	2.00	2.00	2.00
nanotriangle	5.86	4.73	3.02	4.19	0.66	1.90
bow-tie	4.01	1.72	5.50	5.89	1.16	0.67
monopod	2.89	1.78	5.06	3.01	1.83	1.09
bipod	2.95	3.62	5.78	5.82	0.74	1.96
nanoarrow	4.83	2.30	4.66	1.74	1.53	0.77
tripod	5.94	0.92	2.20	0.99	0.65	1.73
tetrapod	7.92	1.65	2.10	2.83	0.61	1.53
pentapod	4.85	1.51	5.23	4.02	1.03	1.27
hexapod	6.00	1.37	5.94	3.58	1.50	2.00

group them into three families, besides the sphere, our optimization domain contains polygonal particles (e.g., nanosquare, nanodisk, nanotriangle, bow-tie particle) and branched particles (e.g., monopod, bipod, nanoarrow, tripod, tetrapod, pentapod, hexapod). By continuously varying the parameters of the superformula, we are able to smoothly transform any shape of Figure 2 into another. It is worth pointing out that shape-controlled spheres and polygonal nanoparticles can be synthesized using both chemical methods^{36–41} such as seed-mediated, light-mediated growth, and polyol process and with electron beam lithography (see, for

instance, ref 42 for nanorods, ref 43 for disks and triangles, and ref 44 for gapless bow-ties). Moreover, the seed-mediated method is one of the most useful chemical approaches for the preparation of branched structures,^{45–49} together with electron beam lithography.⁵⁰ At every step of the optimization process triangular surface meshes of the superformula are automatically generated using the “3D Surface Mesh Generation” package⁵¹ of the Computational Geometry Algorithms Library (CGAL).⁵²

DIRECT ELECTROMAGNETIC PROBLEM

In order to perform the inverse design, a solver of the direct electromagnetic problem is required. The desired solver should be at the same time fast, because it has to be executed a large number of times in a standard global optimization algorithm, yet accurate. The latter requirement is particularly compelling since we are interested in the accurate evaluation of electric field in the near-zone of a plasmonic particle, which is usually not easy to achieve if compared to any far-field quantity.¹⁶

For instance, the FDTD method, although widely used in the analysis of plasmonic structures, appears to be inadequate when high accuracy is required.^{9,10} The FDTD method, with a regular square grid, not only poorly approximates arbitrary boundaries, but also suffers from staircasing effects, which drastically reduce its numerical accuracy.⁹ In addition, spurious solutions can be introduced by the well-known numerical dispersion of the algorithm.¹¹ Furthermore, the poor performances of FDTD are exacerbated when strong field localization is present.¹⁰

On the contrary, electromagnetic surface integral formulations¹⁴ (SIE), although they are only applicable to piecewise uniform materials, are particularly efficient because they only require a surface discretization without sacrificing the near-field accuracy. Thus, we reformulated the electromagnetic problem given by eqs 4 and 5 in terms of Surface Integral Equations (SIE). In particular, we used the JMCFIE formulation.¹⁵ We numerically solved this formulation using the Method of Moments (MoM) with the Rao-Wilton-Glisson (RWG) basis functions.⁵³ We also managed the weak singularities with the techniques described in ref 54. A detailed analysis of the accuracy of the local fields in proximity of metal nanoparticles calculated by the JMCFIE formulation can be found in ref 16.

OPTIMIZATION

The averaged field enhancement g is a time-consuming quantity to evaluate accurately even using the SIE solver. Unfortunately, many standard global optimization algorithms, including genetic algorithms, particle-swarm optimization or simulated annealing are designed for objective functions that are inexpensive to evaluate.⁵⁵ Therefore, we need an efficient algorithm, namely, an algorithm that requires less objective function evaluations, and that carefully chooses where to evaluate it to maximize the information gained at every step. In particular, the Efficient Global Optimization (EGO) is a global optimization algorithm based on response surface surrogates that satisfy both requirements.^{12,13}

The procedure of the EGO algorithm follows the steps summarized in the flowchart shown in Figure 3. First, we construct a tentative Gaussian process (GP) model of the objective function g defined in eq 6, that will be refined during the subsequent iterative process. The GP is a model that closely mimics the behavior of the average electric field enhancement g as a function of the superformula parameters, being able to provide an estimate of the value of g and the corresponding

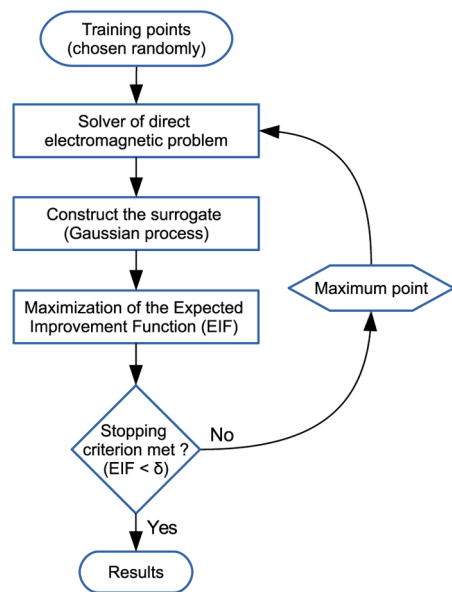


Figure 3. Flowchart of the EGO algorithm scheme for the solution of inverse design problems.

uncertainty with a reduced computational burden. We build it based on a set of $N = 36$ sample points, called training points, belonging to the search space spanned by the superformula parameters and on the corresponding real values of g evaluated by the direct SIE solver. Then, we start the iterative process. At each iteration, we maximize a quantity called Expected Improvement Function (EIF), using a deterministic global optimization algorithm. The function EIF is defined as the expectation that any point in the search space will improve the current optimal solution, and it is estimated based on the expected values of g and of the corresponding uncertainties obtained by the GP model.¹³ Thus, we choose the point at which the EIF is maximized as an additional training point for the GP. Therefore, EGO balances between exploring areas of the search space where good solutions have been found and area where the uncertainty is high to refine the GP model. When the value of EIF is sufficiently small, the iteration process is stopped. We employ the software DAKOTA¹³ developed at Sandia National Laboratories to implement EGO.

RESULTS

We now present the inverse design of metal nanoparticles that maximize the value of g when excited by a monochromatic plane-wave of unit intensity, linearly polarized along the x -axis and propagating along the z -axis.

GOLD

First, we perform the inverse design of gold nanoparticles at different wavelengths λ within the range [400, 900] nm. The gold dispersion has been modeled by interpolating the experimental data of Johnson and Christy.⁵⁶ The superformula parameters obtained by the EGO algorithm are listed in Table 2. The corresponding shapes are shown in Figure 4a, together with the $\|\mathbf{E}\|$ -field distribution on Σ . Next, in Figure 4b, we plot the achieved optimal values of g as a function of the wavelength λ . In the last panel, for each of the shapes shown in panel (a), we numerically calculate, using the SIE method, the g spectrum as a function of the incident wavelength.

The achieved optimal shapes at $\lambda = 400$ and 500 nm, shown in the subpanels of Figure 4a labeled with a red square and a blue circle, resemble nanorods and feature $g = 2.0$ and 2.5, respectively, as listed in Table 2. It is also apparent from the corresponding g spectra shown with red and blue curves in Figure 4c that we are in the tail of the plasmonic resonance, being the degrees of freedom of the geometry not sufficient to blue-shift the plasmonic resonant wavelength to $\lambda = 400$ and 500 nm due to the material constraint. Next, at 600 nm, the optimal shape, shown in subpanel Figure 4a (green triangle), still comes closer to a nanorod, although slightly perturbed by a narrowing of its transverse width, with a longitudinal length increased if compared to the subpanels identified with a red square and a blue circle. Moreover, the corresponding g spectrum, shown with a green curve in Figure 4c, has its peak exactly at the prescribed optimization wavelength; this fact has a beneficial effect on the achieved value of g , which increases to 9.6. At 700 nm the optimal shape is the tripod labeled with a cyan diamond, featuring three hot spots at the end of each arm. As apparent from Figure 4b its value of g , that is 20.2, is the highest among all the investigated wavelengths. As in the previous scenario, the cyan curve in Figure 4c demonstrates that the EGO algorithm exactly tunes the plasmonic resonant peak to the prescribed wavelength, that is, 700 nm. In Figure 4a, we show that the optimal shape obtained at 800 nm and identified with a magenta star is a gapless bow-tie, but the obtained value of g decreases with respect to the previous case. This fact demonstrates that although the plasmonic resonance can be easily red-shifted by acting on the shape, the optimum performance nevertheless suffers a detrimental effect. In the subpanel of Figure 4a labeled with a yellow inverted triangle we show that the optimal shape at 900 nm is again a tripod with longer arms with respect to the case at 700 nm. We conclude from the analysis of Figure 4c that, besides the first two scenarios, the g spectra of the optimal shapes we found always reach their peak at the prescribed optimization wavelength. This result is a natural consequence of the maximization of g .

Table 2. Superformula Parameters Describing the Inverse-Designed Au Nanoparticles with Optimal g

λ (nm)	$m^{(\phi)}$	$n_1^{(\phi)}$	$n_2^{(\phi)}$	$n_3^{(\phi)}$	$a^{(\phi)}$	$b^{(\phi)}$	η (nm)	g
400	4.64	4.04	4.24	2.90	1.50	0.92	26	2.0
500	4.20	4.15	2.49	4.84	1.28	0.72	30	2.5
600	4.38	2.62	4.91	3.37	1.26	0.50	36	9.6
650	6.57	6.0	5.92	5.99	1.88	0.50	37	11.6
700	6.10	3.4	4.33	4.25	2.0	0.50	25	20.2
750	5.94	1.80	2.88	3.85	0.50	1.39	51	9.51
800	4.18	2.73	4.71	5.71	1.67	0.50	38	13.7
850	8.0	2.49	6.0	5.43	1.71	7.75	25	13.83
900	6.14	2.70	6.0	4.52	2.0	0.83	25	15.0

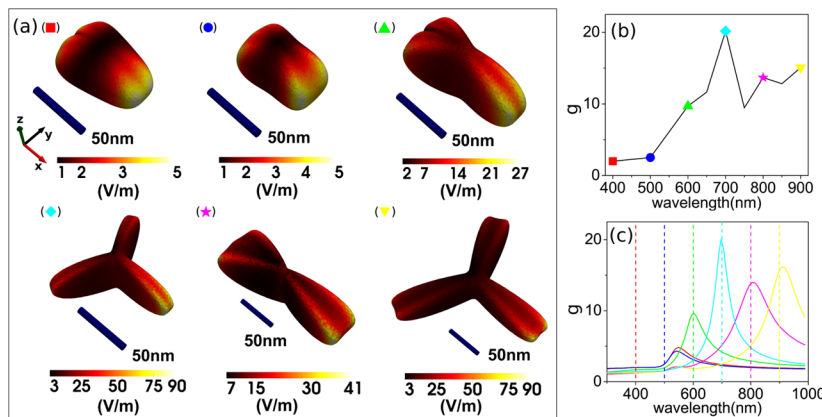


Figure 4. (a) Inverse-designed Au nanoparticles and corresponding $\|\mathbf{E}\|$ -field distribution (V/m, linear scale) on Σ . The particles are excited by a x -polarized plane wave of unit electric field magnitude (1 V/m) propagating along the z -axis at wavelength (red square) 400 nm, (blue circle) 500 nm, (green triangle) 600 nm, (cyan diamond) 700 nm, (magenta star) 800 nm, (yellow inverted triangle) 900 nm. All scale bars correspond to 50 nm. (b) Optimal value of g as a function of the incident wavelength. (c) g spectra calculated for the optimal shapes as a function of the incident wavelength; each curve corresponds to the particle of panel (a) labeled by the symbol of corresponding color.

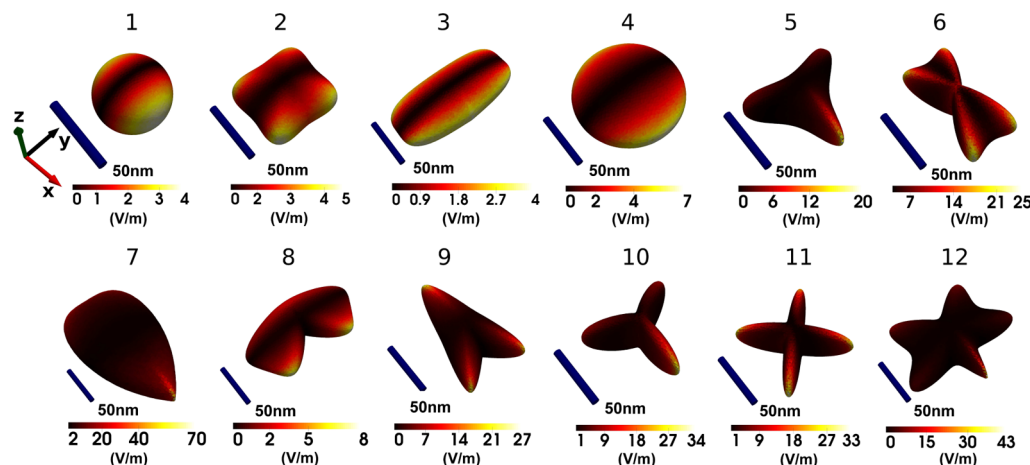


Figure 5. $\|\mathbf{E}\|$ -field distribution (V/m, linear scale) on the exemplificative shapes introduced in Figure 2 with $\eta = 25$ nm, namely, (1) nanosphere with $g = 1.8$, (2) nanosquare with 2.1, (3) nanorod with 1.7, (4) nanocylinder with 2.4, (5) nanotriangle with 2.4, (6) bow-tie with 8.6, (7) monopod with 7.2, (8) bipod with 1.8, (9) nanoarrow with 4.4, (10) tripod with 5.0, (11) tetrapod with 6.8, (12) pentapod with 2.8. The particles are excited by a x -polarized plane wave of unit electric field magnitude (1 V/m), propagating along the z -axis at wavelength 700 nm. All scale bars correspond to 50 nm.

and further supports the effectiveness of our method. Beside the finding of optimal shapes, this study also establishes, in the broad domain of shapes spanned by the superformula, an upper bound for the average electric field achievable on the surface of an isolated particle, which is $g = 20.2$ for Au. This is of great practical importance because it is directly related to the maximum performances accessible by the plasmonic devices based on noninteracting metal nanoparticles.

In order to support the results found so far with the EGO algorithm, we compare the achieved optima with the values of g calculated for several canonical shapes found in the literature^{36–50} and described in terms of the superformula parameters. We carry out this analysis using the direct SIE electromagnetic solver for the case of gold at 700 nm, where we found the peak value of g (see Figure 4b). We calculate the values of g for the shapes 1–12 shown in Figure 2 with $\eta = 25$ nm, and we plot the corresponding $\|\mathbf{E}\|$ -field distribution on Σ in Figure 5. Among the considered tentative shapes, the best ones are in the order the gapless bow-tie ($g = 8.6$), monopod ($g = 7.2$), and tetrapod ($g = 6.8$). We conclude that the maximum

value of the g obtained in Figure 5, that is 8.6, is much lower than the maximum obtained using the inverse design strategy (i.e., 20.2). Figure 5 is also instrumental to show that, although the maximum and the averaged field enhancement g on Σ are correlated, high values of g do not always guarantee high values of maximum field enhancement and vice versa. For instance, among the particles shown in Figure 5, the shape #6 features the highest value of g , but has a pretty low value of the maximum enhancement, as apparent from the colorbar; on the contrary the shape #7, which features a much higher value of maximum enhancement, has a lower value of g than shape #6. In fact, in the shape #7, high electric fields play a minor role in the calculation of g by eq 6 because they are only localized on a very small surface area in the neighborhood of the nanoarrow's three tips; whereas shape #6 shows a lower but more distributed electric field magnitude, which guarantees a higher average.

SILVER

We now present the results of the inverse design of silver (Ag) nanoparticle within the spectral range [200, 500] nm. We used the Ag permittivity obtained by interpolating the experimental data of Johnson and Christy.⁵⁶ The parameters of the superformula defining the optimal scatterer obtained by the EGO method are listed in **Table 3** for several wavelengths; the

Table 3. Superformula Parameters Describing the Inverse-Designed Ag Nanoparticles with Optimal g

λ (nm)	$m^{(\phi)}$	$n_1^{(\phi)}$	$n_2^{(\phi)}$	$n_3^{(\phi)}$	$a^{(\phi)}$	$b^{(\phi)}$	η (nm)	g
200	1.01	4.43	4.26	2.00	0.50	0.73	25.0	1.6
250	1.01	4.04	4.26	5.43	0.82	0.70	25.0	1.6
300	3.32	2.50	3.68	0.76	0.72	0.51	32.7	1.4
325	3.32	0.93	4.26	1.34	0.50	0.50	25	1.8
350	1.01	3.66	4.26	1.90	0.50	0.50	25	10
375	3.80	4.43	0.76	3.76	0.50	0.50	25	19
400	4.38	5.71	0.89	6.00	1.39	0.50	25	22
450	7.58	6.00	3.68	3.27	0.52	2.00	26	16

corresponding $\|\mathbf{E}\|$ -field distributions on Σ are shown in **Figure 6a**. Additionally, in **Figure 6b**, we plot the achieved optimal values of g as a function of the optimization wavelength λ . In the panel (c), we show the g spectrum of the found optimal shapes as a function of the incident wavelength. At the deep-ultraviolet wavelengths, $\lambda = 250$ and 300 nm, the optimal shapes resulting from the optimization process are approximatively nanospheres, as shown in the subpanels of **Figure 6a** labeled with a red square and a blue circle, respectively. Unfortunately, at these wavelengths the silver does not exhibit good plasmonic properties and this is reflected in modest values of g , namely, 1.6 and 1.4, respectively. In facts, we are in the tail of the plasmonic resonant curve, as apparent if we examine the corresponding g spectra shown with red and blue curves in **Figure 6c**. Increasing the wavelength to 350 nm the optimal shape is the nanorod identified with a green triangle in **Figure 6a**, which features a much higher value of g , that is 10. At 375 nm the inverse design algorithm returns approximately a prolate spheroids with $g = 19$, identified in **Figure 6a** with a cyan diamond. The parameters of the superformula defining the optimal scatterer obtained by the EGO method are listed in **Table 3** for several wavelengths; the

nm the inverse design algorithm returns approximately a prolate spheroids with $g = 19$, identified in **Figure 6a** with a cyan diamond. Then, the objective function reaches its peak at $\lambda = 400$ nm, where the nanorod labeled with a magenta star exhibits $g = 22$, which is the highest value that we are able to achieve for Ag, as shown in **Figure 6b**, and only slightly surpasses the maximum value obtained for gold. Finally, at 450 nm, the tetrapod identified with a yellow inverted triangle in **Figure 6a** maximizes the value of g . Moreover, it is apparent that the g spectra of the optimal shapes, shown in **Figure 6c**, feature their peak values at the prescribed optimization wavelength, in all but the first two cases. As in the case of Au, this fact further corroborates the EGO efficacy for the design of Ag nanoparticles. It is worth noting that the scale factor η of the optimized particles, shown in **Table 3**, assumes in most of the investigated scenarios the minimum allowed value prescribed by the assigned constraint of **eq 11**. This fact suggests that by relaxing the lower bound of η we may obtain different optimal shapes with higher value of g . However, this will results in particles too small to be fabricated with the current technology, and therefore outside the scope of this study.

ALUMINUM

As apparent from **Figures 4b** and **6b** gold and silver do not exhibit satisfactory plasmon properties in the ultraviolet spectral range (UV), as consistently demonstrated by previous studies (e.g., ref 57). Unlike coinage metals, aluminum (Al) holds great potential to extend the plasmonic properties into the ultraviolet spectral range,^{58,59} bearing the promise of enhancing the emission of fluorophores,^{60–64} biomolecules⁶⁵ and UV-light-emitting diodes (LEDs) based on III–V nitride semiconductors, such as GaN or InGaN. For this reason, we also perform the inverse design of Al nanoparticle within the UV spectral range [100, 400] nm, using the Al permittivity measured by Palik.⁶⁶

The results of the EGO algorithm are summarized in **Table 4**; the corresponding shapes are represented in **Figure 7a**, where the corresponding $\|\mathbf{E}\|$ -field distributions on Σ are also shown.

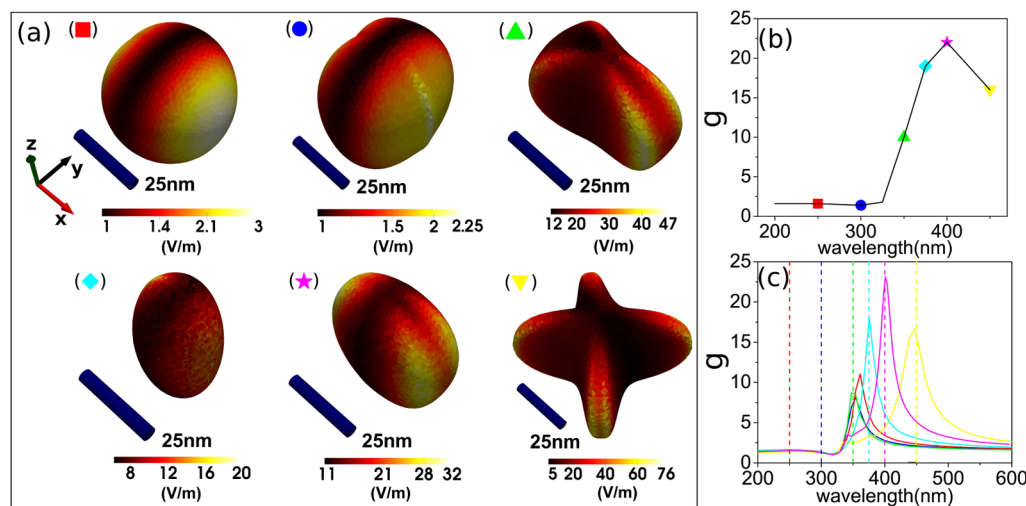


Figure 6. (a) Inverse-designed Ag nanoparticles and corresponding $\|\mathbf{E}\|$ distribution (V/m, linear scale) on Σ . The particles are excited by a x -polarized plane wave of unit electric field magnitude (1 V/m), propagating along the z -axis at wavelength (red square) 250 nm, (blue circle) 300 nm, (green triangle) 350 nm, (cyan diamond) 375 nm, (magenta star) 400 nm, (yellow inverted triangle) 450 nm. All scale bars correspond to 25 nm. (b) Optimum value of g as a function of the incident wavelength. (c) g spectra calculated for the optimal shapes as a function of the incident wavelength; each curve corresponds to the particle of panel (a) labeled by the symbol of corresponding color.

Table 4. Superformula Parameters Describing the Inverse-Designed Al Nanoparticles with Optimal g

λ (nm)	$m^{(\phi)}$	$n_1^{(\phi)}$	$n_2^{(\phi)}$	$n_3^{(\phi)}$	$a^{(\phi)}$	$b^{(\phi)}$	η (nm)	g
100	8.00	1.56	2.50	0.76	0.50	0.96	25	4.9
150	4.10	1.84	2.73	3.57	0.50	0.50	25	11.4
200	5.94	0.87	0.76	6.00	0.50	0.80	25	7.8
250	6.45	3.37	3.33	6.00	1.06	0.51	25	6.4
300	8.00	4.35	5.43	4.26	0.50	1.47	25	6.4
350	4.10	4.25	5.72	6.00	1.50	0.50	25	6.9
400	4.38	3.03	5.25	6.00	1.43	0.50	28	6.4

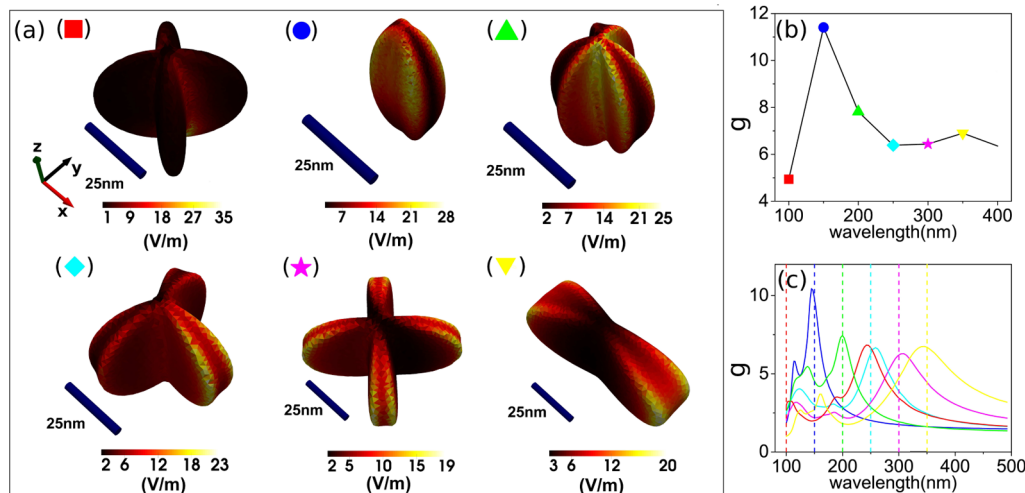


Figure 7. (a) Inverse-designed Al nanoparticles and corresponding $\|E\|$ distribution (V/m , linear scale) on Σ . The particles are excited by a x -polarized plane wave of unit electric field magnitude (1 V/m), propagating along the z -axis at wavelength (red square) 100 nm, (blue circle) 150 nm, (green triangle) 200 nm, (cyan diamond) 250 nm, (magenta star) 300 nm, (yellow inverted triangle) 350 nm. All scale bars correspond to 25 nm. (b) Optimum value of g as a function of the incident wavelength. (c) g spectra calculated for the optimal shapes as a function of the incident wavelength; each curve corresponds to the particle of panel (a) labeled by the symbol of corresponding color.

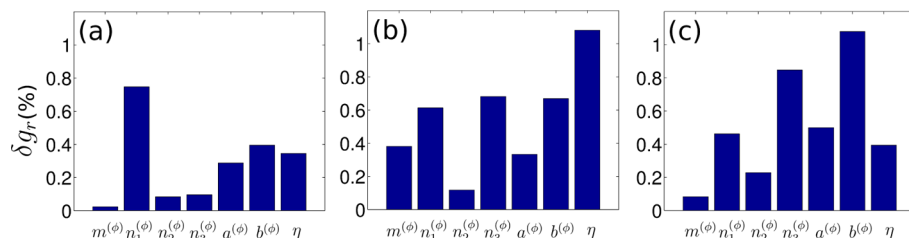


Figure 8. Percentage changes of g resulting from a 0.5% increase of the seven superformula parameters in the case of (a) gold, (b) silver, and (c) aluminum.

The optimal shapes are, in order of complexity, a prolate particle for $\lambda = 150$ nm (identified with a blue circle in Figure 7(a)); a bow-tie particle for $\lambda = 350$ nm (yellow inverted triangle); a tripod for $\lambda = 200$ (green triangle) and $\lambda = 250$ (cyan diamond); a tetrapod for $\lambda = 100$ nm (red square) and $\lambda = 300$ nm (magenta star). Similarly to Ag particles, in all but one investigated scenarios, the Al optimized particles assume a value of the scale factor η equal to the minimum value allowed by eq 11. Therefore, also in this case by relaxing the lower bound of the η we may obtain differently shaped particle with better performances, which, however, would be too small to be manufactured with the current technology. In Figure 7b we plot the optimum values of g as a function of the incident wavelength λ . The highest value of g of 12 is obtained for $\lambda = 150$ nm. This fact proves the suitability of Al for UV applications even if the quality of its plasmon resonance in terms of g appears to be worse than the analogous resonances

of Ag and Au in the visible. Moreover, the fact that, besides the $\lambda = 100$ nm scenario, the g spectra of the optimal Al shapes, calculated in Figure 7c, are always peaked at the prescribed optimization wavelength further validates the EGO inverse design.

In conclusion, for Au and Al (Figures 4a and 7a) branched particles are a very common solution of the inverse design problem; contrarily, the Ag optimization give rise to more compact shapes like spheres and ellipsoids. This difference may be traced back to the different dispersion of the three materials, since the Ag has a higher quality factor, that is, $Q(\lambda) = \Re\{\epsilon_i(\lambda)\}/\Im\{\epsilon_i(\lambda)\}$, than Au and Al (see, for instance, ref 67 for a comparison of the quality factors Q as a function of the frequency).

However, any practical implementation of this approach requires the achieved optimal value of g to be robust against manufacturing uncertainty. Thus, we represent the uncertainty

on the particle's shape as a deterministic variation of the superformula parameters within the neighborhood of the optimal value, and we determine the corresponding suboptimal value of average field enhancement \tilde{g} on Σ . We then characterize the robustness of our solution using the relative difference between the optimal and suboptimal values of averaged electric field:

$$\delta g_r = \frac{|g - \tilde{g}|}{g} \quad (12)$$

In particular, we investigated the robustness of the optimal shapes featuring the highest value of g for each material, namely, the optimal Au particle at 700 nm, labeled with a blue diamond in Figure 4a; the optimal Ag particle at 400 nm, labeled with a magenta star in Figure 6a; and the optimal Al particle at 150 nm, labeled with a blue circle in Figure 7a. The corresponding seven parameter describing the superformula, listed in Tables 2, 3, and 4, are increased by 0.5% one at the time, and the corresponding values of δg_r are shown in Figure 8 for the three investigated cases. It is apparent that, irrespectively to the material, a 0.5% variation of any of the superformula parameters determines, in the worst case, a small variation (i.e., $\delta g_r \approx 1\%$) of the electric field average on Σ . This fact demonstrates that the performance of the optimized particles is relatively immune to small geometrical variations of the particle.

CONCLUSIONS

We have developed and implemented a method to inverse-design three-dimensional plasmonic nanoparticles. Contrary to existing inverse-design strategies, our method allows the optimization of three-dimensional nanoparticles searching within a continuous parameter space, and exploiting a full-wave integral electromagnetic solver, which is accurate and reliable in the near-field region. Our approach could be used to optimize either far-field or near-field quantities and easily allows to incorporate the limitations of fabrication as optimization constraints. Specifically, in this paper, we demonstrate its effectiveness by designing the nanoparticle's shape in order to maximize the field enhancement averaged over its surface, which plays a fundamental role in the surface enhanced Raman scattering and for the subwavelength focusing of light. Design criteria of nanoparticle's shape and size are obtained for different plasmonic materials. In particular, our optimizations demonstrate that branched particles are the preferred shape for materials with low quality factor, such as gold and aluminum. Conversely, for silver nanoparticles featuring an higher quality factor, the algorithm selects more compact shapes with higher values of averaged field enhancement. This study also provides an upper bound for the average surface electric field which can be obtained for an isolated particle of Au, Ag, and Al, which is directly related to the maximum performances achievable by the plasmonic devices based on the optimized particle, for example, SERS substrates. We also show the reliability and robustness of the identified optimal solutions against morphological fluctuations. Furthermore, the extension of the present method to design the geometry of arrays of several interacting particles maximizing multiple objective functions is straightforward. Our results demonstrate that the use of optimization algorithms in combination with the rigorous surface integral equation method represents a practical venue for device level engineering of metal nanostructures, providing

unanticipated solutions to numerous exciting problems in plasmonics.

AUTHOR INFORMATION

Corresponding Authors

*E-mail: carlo.forestiere@unina.it.
*E-mail: kirby@cs.utah.edu.
*E-mail: dalnegro@bu.edu.

Notes

The authors declare no competing financial interest.

ACKNOWLEDGMENTS

This work was supported by the Army Research Laboratory under Cooperative Agreement Number W911NF-12-2-0023. UofU authors would like to acknowledge the University of Utah MRSEC (National Science Foundation Grant #DMR 11-21252) for the support through the Seed Grant Program. The views and conclusions contained in this document are those of the authors and should not be interpreted as representing the official policies, either expressed or implied, of the Army Research Laboratory or the U.S. Government.

REFERENCES

- Prodan, E.; Radloff, C.; Halas, N. J.; Nordlander, P. A Hybridization Model for the Plasmon Response of Complex Nanostructures. *Science* **2003**, *302*, 419–422.
- Stockman, M. I. Nanofocusing of Optical Energy in Tapered Plasmonic Waveguides. *Phys. Rev. Lett.* **2004**, *93*, 137404.
- Forestiere, C.; Donelli, M.; Walsh, G. F.; Zeni, E.; Miano, G.; Dal Negro, L. Particle-swarm optimization of broadband nanoplasmonic arrays. *Opt. Lett.* **2010**, *35*, 133–135.
- Ginzburg, P.; Berkovitch, N.; Nevet, A.; Shor, I.; Orenstein, M. Resonances On-Demand for Plasmonic Nano-Particles. *Nano Lett.* **2011**, *11*, 2329–2333.
- Forestiere, C.; Pasquale, A. J.; Capretti, A.; Miano, G.; Tamburrino, A.; Lee, S. Y.; Reinhard, B. M.; Dal Negro, L. Genetically Engineered Plasmonic Nanoarrays. *Nano Lett.* **2012**, *12*, 2037–2044.
- Tassadit, A.; Macías, D.; Sánchez-Gil, J. A.; Adam, P.-M.; Rodríguez-Oliveros, R. Metal nanostars: Stochastic optimization of resonant scattering properties. *Superlattices Microstruct.* **2011**, *49*, 288–293.
- Macías, D.; Adam, P.-M.; Ruiz-Cortés, V.; Rodríguez-Oliveros, R.; Sánchez-Gil, J. A. Heuristic optimization for the design of plasmonic nanowires with specific resonant and scattering properties. *Opt. Express* **2012**, *20*, 13146–13163.
- Feichtner, T.; Selig, O.; Kiunke, M.; Hecht, B. Evolutionary Optimization of Optical Antennas. *Phys. Rev. Lett.* **2012**, *109*, 127701.
- Smajic, J.; Hafner, C.; Raguin, L.; Tavzashvili, K.; Mishrikey, M. Comparison of Numerical Methods for the Analysis of Plasmonic Structures. *J. Comput. Theor. Nanosci.* **2009**, *6*, 763.
- Hoffmann, J.; Hafner, C.; Leidenberger, P.; Hesselbarth, J.; Burger, S. Comparison of electromagnetic field solvers for the 3D analysis of plasmonic nanoantennas. SPIE Europe Optical Metrology, Munich, Germany, June 15, 2009, SPIE, 2009; 73900J.
- Yee, K.; Chen, J. The finite-difference time-domain (FDTD) and the finite-volume time-domain (FVTD) methods in solving Maxwell's equations. *IEEE Trans. Antennas Propag.* **1997**, *45*, 354–363.
- Jones, D.; Schonlau, M.; Welch, W. Efficient Global Optimization of Expensive Black-Box Functions. *J. Global Optim.* **1998**, *13*, 455–492.
- Adams, B.; Ebeida, M.; Eldred, M.; Jakeman, J. S.; Swiler, L.; Vigil, D.; Wildey, T.; Bohnhoff, W.; Dalbey, K.; Eddy, T. H.; Bauan, L.; Hough, P.; Dakota, A. *Users Manual: Multilevel Parallel Object-Oriented Framework for Design Optimization, Parameter Estimation, Uncertainty Quantification, and Sensitivity Analysis*, Version 6.1; Sandia National Laboratories: Albuquerque, NM, 2014.

(14) Harrington, R. F.; Harrington, J. L. *Field Computation by Moment Methods*; Oxford University Press, 1996.

(15) Yla-Oijala, P.; Taskinen, M. Application of combined field Integral equation for electromagnetic scattering by dielectric and composite objects. *IEEE Trans. Antennas Propag.* **2005**, *53*, 1168–1173.

(16) Forestiere, C.; Iadarola, G.; Rubinacci, G.; Tamburrino, A.; Dal Negro, L.; Miano, G. Surface integral formulations for the design of plasmonic nanostructures. *J. Opt. Soc. Am. A* **2012**, *29*, 2314–2327.

(17) Gielis, J. A generic geometric transformation that unifies a wide range of natural and abstract shapes. *Am. J. Bot.* **2003**, *90*, 333–338.

(18) Moskovits, M. In *Surface-Enhanced Raman Scattering: Physics and Applications*; Kneipp, K., Moskovits, M., Kneipp, H., Eds.; Springer, 2006; Chapter 1, pp 1–17.

(19) Novotny, L.; Hecht, B. *Principles of Nano-optics*; Cambridge University Press, 2006.

(20) Gersten, J. I. The effect of surface roughness on surface enhanced Raman scattering. *J. Chem. Phys.* **1980**, *72*, 5779–5780.

(21) Gersten, J.; Nitzan, A. Electromagnetic theory of enhanced Raman scattering by molecules adsorbed on rough surfaces. *J. Chem. Phys.* **1980**, *73*, 3023–3037.

(22) Gersten, J.; Nitzan, A. Spectroscopic properties of molecules interacting with small dielectric particles. *J. Chem. Phys.* **1981**, *75*, 1139–1152.

(23) Kauranen, M.; Zayats, A. V. Nonlinear plasmonics. *Nat. Photonics* **2012**, *6*, 737–748.

(24) Tang, L.; Kocabas, S. E.; Latif, S.; Okyay, A. K.; Ly-Gagnon, D.; Saraswat, K. C.; Miller, D. A. B. Nanometre-scale germanium photodetector enhanced by a near-infrared dipole antenna. *Nat. Photonics* **2008**, *2*, 226–229.

(25) Atwater, H. A.; Polman, A. Plasmonics for improved photovoltaic devices. *Nat. Mater.* **2010**, *9*, 205–213.

(26) Grigorenko, A. N.; Roberts, N. W.; Dickinson, M. R.; Zhan, Y. Nanometric optical tweezers based on nanostructured substrates. *Nat. Photonics* **2008**, *2*, 365–370.

(27) Nikolajsen, T.; Leosson, K.; Bozhevolnyi, S. I. Surface plasmon polariton based modulators and switches operating at telecom wavelengths. *Appl. Phys. Lett.* **2004**, *85*, 5833–5835.

(28) Schuller, J. A.; Taubner, T.; Brongersma, M. Optical antenna thermal emitters. *Nat. Photonics* **2009**, *3*, 658–661.

(29) Kawata, S.; Inouye, Y.; Verma, P. Plasmonic for near-field nano-imaging and superlensing. *Nat. Photonics* **2009**, *3*, 388–394.

(30) Pan, L.; Bogy, D. B. Data storage: Heat-assisted magnetic recording. *Nat. Photonics* **2009**, *3*, 189–190.

(31) Engheta, N.; Ziolkowski, R. W. *Electromagnetic Metamaterials: Physics and Engineering Explorations*; Wiley & Sons: New York, 2006.

(32) Gielis, J.; Haesen, S.; Verstraelen, L. Universal shapes: from the supereggs of Piet Hein to the cosmic egg of George Lemaître. *Kragujevac J. Math.* **2005**, *28*, 55–67.

(33) Gielis, J. Method and apparatus for synthesizing and analyzing patterns utilizing novel “super-formula” operator. U.S. Patent US7,620,527, 2009.

(34) Paraforou, V. Design and full-wave analysis of supershaped patch antennas. *Ph.D. Dissertation*, Delft University of Technology, 2013.

(35) Rodríguez-Oliveros, R.; Sánchez-Gil, J. A. Localized surface-plasmon resonances on single and coupled nanoparticles through surface integral equations for flexible surfaces. *Opt. Express* **2011**, *19*, 12208–12219.

(36) Jin, R.; Cao, Y.; Mirkin, C. A.; Kelly, K. L.; Schatz, G. C.; Zheng, J. G. Photoinduced Conversion of Silver Nanospheres to Nanoprisms. *Science* **2001**, *294*, 1901–1903.

(37) Wiley, B.; Sun, Y.; Mayers, B.; Xia, Y. Shape-Controlled Synthesis of Metal Nanostructures: The Case of Silver. *Chem. - Eur. J.* **2005**, *11*, 454–463.

(38) Glotzer, S. C.; Solomon, M. J. Anisotropy of building blocks and their assembly into complex structures. *Nat. Mater.* **2007**, *6*, 557–562.

(39) Lu, X.; Rycenga, M.; Skrabalak, S. E.; Wiley, B.; Xia, Y. Chemical Synthesis of Novel Plasmonic Nanoparticles. *Annu. Rev. Phys. Chem.* **2009**, *60*, 167–192.

(40) Funston, A. M.; Novo, C.; Davis, T. J.; Mulvaney, P. Plasmon Coupling of Gold Nanorods at Short Distances and in Different Geometries. *Nano Lett.* **2009**, *9*, 1651–1658.

(41) Rycenga, M.; Cobley, C. M.; Zeng, J.; Li, W.; Moran, C. H.; Zhang, Q.; Qin, D.; Xia, Y. Controlling the Synthesis and Assembly of Silver Nanostructures for Plasmonic Applications. *Chem. Rev.* **2011**, *111*, 3669–3712.

(42) Smythe, E. J.; Cubukcu, E.; Capasso, F. Optical properties of surface plasmon resonances of coupled metallic nanorods. *Opt. Express* **2007**, *15*, 7439–7447.

(43) Gopinath, A.; Boriskina, S. V.; Reinhard, B. M.; Dal Negro, L. Deterministic aperiodic arrays of metal nanoparticles for surface-enhanced Raman scattering (SERS). *Opt. Express* **2009**, *17*, 3741–3753.

(44) Koh, A. L.; Fernández-Domínguez, A. I.; McComb, D. W.; Maier, S. A.; Yang, J. K. W. High-Resolution Mapping of Electron-Beam-Excited Plasmon Modes in Lithographically Defined Gold Nanostructures. *Nano Lett.* **2011**, *11*, 1323–1330.

(45) Chen, S.; Wang, Z. L.; Ballato, J.; Foulger, S. H.; Carroll, D. L. Monopod, Bipod, Tripod, and Tetrapod Gold Nanocrystals. *J. Am. Chem. Soc.* **2003**, *125*, 16186–16187.

(46) Sau, T. K.; Murphy, C. J. Room Temperature, High-Yield Synthesis of Multiple Shapes of Gold Nanoparticles in Aqueous Solution. *J. Am. Chem. Soc.* **2004**, *126*, 8648–8649.

(47) Hao, E.; Bailey, R. C.; Schatz, G. C.; Hupp, J. T.; Li, S. Synthesis and Optical Properties of “Branched” Gold Nanocrystals. *Nano Lett.* **2004**, *4*, 327–330.

(48) Nehl, C. L.; Liao, H.; Hafner, J. H. Optical Properties of Star-Shaped Gold Nanoparticles. *Nano Lett.* **2006**, *6*, 683–688.

(49) Liao, H.-G.; Jiang, Y.-X.; Zhou, Z.-Y.; Chen, S.-P.; Sun, S.-G. Shape-Controlled Synthesis of Gold Nanoparticles in Deep Eutectic Solvents for Studies of Structure-Functionality Relationships in Electrocatalysis. *Angew. Chem., Int. Ed.* **2008**, *47*, 9100–9103.

(50) Chirumamilla, M.; Gopalakrishnan, A.; Toma, A.; Zaccaria, R. P.; Krahne, R. Plasmon resonance tuning in metal nanostars for surface enhanced Raman scattering. *Nanotechnology* **2014**, *25*, 235303.

(51) Rineau, L.; Yvinec, M. *CGAL User and Reference Manual*, 4.6 ed.; CGAL Editorial Board, 2015.

(52) *The CGAL Project, CGAL User and Reference Manual*, 4.6 ed.; CGAL Editorial Board, 2015.

(53) Rao, S.; Wilton, D.; Glisson, A. Electromagnetic scattering by surfaces of arbitrary shape. *IRE Trans. Antennas Propag.* **1982**, *30*, 409–418.

(54) Graglia, R. On the numerical integration of the linear shape functions times the 3-D Green’s function or its gradient on a plane triangle. *IEEE Trans. Antennas Propag.* **1993**, *41*, 1448–1455.

(55) Pintér, J. D. In *Handbook of Global Optimization*; Pardalos, P. M.; Romeijn, H. E., Eds.; Springer: U.S., 2002; Vol. 62, pp 515–569.

(56) Johnson, P. B.; Christy, R. W. Optical Constants of the Noble Metals. *Phys. Rev. B* **1972**, *6*, 4370–4379.

(57) McMahon, J. M.; Schatz, G. C.; Gray, S. K. Plasmonics in the ultraviolet with the poor metals Al, Ga, In, Sn, Tl, Pb, and Bi. *Phys. Chem. Chem. Phys.* **2013**, *15*, 5415–5423.

(58) Knight, M. W.; Liu, L.; Wang, Y.; Brown, L.; Mukherjee, S.; King, N. S.; Everitt, H. O.; Nordlander, P.; Halas, N. J. Aluminum Plasmonic Nanoantennas. *Nano Lett.* **2012**, *12*, 6000–6004.

(59) Schwab, P. M.; Moosmann, C.; Wissert, M. D.; Schmidt, E. W. G.; Ilin, K. S.; Siegel, M.; Lemmer, U.; Eisler, H.-J. Linear and Nonlinear Optical Characterization of Aluminum Nanoantennas. *Nano Lett.* **2013**, *13*, 1535–1540.

(60) Ray, K.; Chowdhury, M. H.; Lakowicz, J. R. Aluminum Nanostructured Films as Substrates for Enhanced Fluorescence in the Ultraviolet-Blue Spectral Region. *Anal. Chem.* **2007**, *79*, 6480–6487.

(61) Chowdhury, M. H.; Ray, K.; Lakowicz, J. R. Use of aluminum films as substrates for enhanced fluorescence in the ultraviolet-blue spectral region. *Proc. SPIE* **2008**, 68690E–68690E.

(62) Chowdhury, M. H.; Ray, K.; Gray, S. K.; Pond, J.; Lakowicz, J. R. Aluminum Nanoparticles as Substrates for Metal-Enhanced Fluorescence in the Ultraviolet for the Label-Free Detection of Biomolecules. *Anal. Chem.* **2009**, *81*, 1397–1403.

(63) Jiao, X.; Blair, S. Optical antenna design for fluorescence enhancement in the ultraviolet. *Opt. Express* **2012**, *20*, 29909–29922.

(64) Forestiere, C.; Handin, A.; Dal Negro, L. Enhancement of Molecular Fluorescence in the UV Spectral Range Using Aluminum Nanoantennas. *Plasmonics* **2014**, *9*, 715–725.

(65) Lakowicz, J. R. *Principles of Fluorescence Spectroscopy*; Springer, 2013.

(66) Palik, E. D. *Handbook of Optical Constants of Solids*; Academic Press, 1998.

(67) Stockman, M. I. Nanoplasmonics: past, present, and glimpse into future. *Opt. Express* **2011**, *19*, 22029–22106.